THE JOURNAL OF PHYSICAL CHEMISTRY C

pubs.acs.org/JPCC Article

Identification of Efficient Active Sites in Nitrogen-Doped Carbon Nanotubes for Oxygen Reduction Reaction

Zhengyu Xu, Ziyu Zhou, Boyang Li, Guofeng Wang,* and Paul W. Leu*

Cite This: J. Phys. Chem. C 2020, 124, 8689–8696 Read Online

ACCESS | Metrics & More | Article Recommendations | Supporting Information

ABSTRACT: Nitrogen-doped carbon nanotubes (NCNTs) have demonstrated great promise as an electrocatalyst alternative to platinum for oxygen reduction reaction (ORR). However, there is much disagreement regarding which N doping sites are most desirable for the reaction. Here, we report an experimental and computational study to identify the efficient active sites in NCNTs for ORR in alkaline media. In our experiments, we synthesized NCNTs of similar overall N content (~4.1%) and carbon matrix but varying percentages of different types of N doping species. Our results reveal a positive correlation between ORR activity and the content of graphitic N doping. Furthermore, we performed density functional theory calculations to predict the free energy evolution of ORR on various N doping sites in NCNTs. Our computational results also indicate that graphitic N doping sites exhibit higher thermodynamic limiting potential for ORR than pyridinic N doping sites. Our combined experimental and theoretical study concludes that graphitic N doping sites are more efficient for ORR than pyridinic N doping in NCNTs.

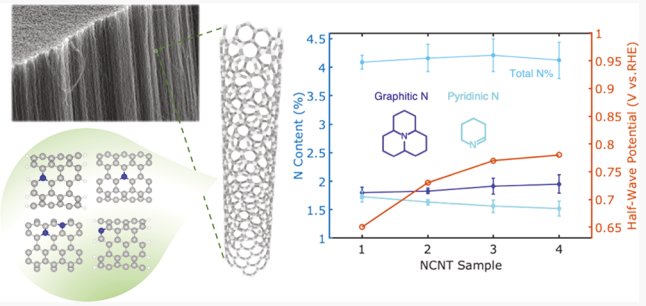

1. INTRODUCTION

Platinum (Pt)-based electrocatalysts exhibit high catalytic performance for oxygen reduction reaction (ORR) as the cathode of fuel cells.[1,2] However, Pt is a precious metal with high cost that hampers its wide deployment in fuel cell technology.[3−5] Hence, extensive research efforts have been devoted to the discovery and development of alternative non-precious metal and metal-free catalysts for ORR.[6−9] Nitrogen-doped carbon nanomaterials, such as nitrogen-doped carbon nanotubes (NCNTs), in particular, have drawn great interest due to their low cost and promising ORR activity.[3,10−14] However, N-doped carbon catalysts have yet to exhibit performance comparable to that of Pt-based catalysts.[10,15−17] To improve the catalytic performance of NCNTs, knowledge about the optimal chemical nature of the active sites in these materials for ORR is crucial but currently lacking.

Although it is well-recognized that increasing overall N content leads to improved performance of the N-doped carbon nanomaterials,[17,18] there have been two main different points of view with regard to what the most active N doping sites are in this type of ORR electrocatalyst. Some researchers have suggested that pyridinic-type N doping is primarily responsible for the observed ORR activity,[15,16,19−22] whereas others have suggested that graphite-like N doping accounts for their excellent electrochemical activity.[23−27] It should also be noted that there are many investigations on dopant-free materials such as hybrid nanospheres with CNTs and graphene[28] and edge-rich graphene.[29] While these studies on carbon nanomaterials may have some similarities in their results with N-doped CNTs, specific studies focused on N-doped CNTs as catalyst are nevertheless necessary. Distinct from other carbon nanomaterials, CNTs show a high degree crystallinity,[30] geometric curvature, hollow configurations, and different chirality. These features and properties can be used to effectively tailor their catalytic performance.[31−34] Moreover, many techniques, such as the furnace-moving method and water-assisted synthesis, have been developed and maybe available for large-scale production of CNT-based catalysts.[35,36]

At least two experimental studies have been specifically aimed to identify the ORR active sites in NCNT catalysts. Using a variety of polymer precursors, Rao et al. synthesized vertically aligned NCNTs without any metal impurities and with different surface N concentrations.[19] They further determined the atomic percentages of pyridinic, pyrrolic, and graphitic N doping from X-ray photoelectron spectroscopy (XPS) and observed that the increase in ORR activity was most closely correlated to pyridinic N content. On the basis of this observation, they concluded that pyridinic N sites are the most active sites for ORR. In contrast, Sharifi et al. obtained

Received: November 27, 2019
Revised: February 17, 2020
Published: February 26, 2020

https://dx.doi.org/10.1021/acs.jpcc.9b11090
J. Phys. Chem. C 2020, 124, 8689–8696

their samples through thermal annealing of NCNTs at different temperatures ranging from 500 to 1000 °C to transform pyrrolic N into pyridinic N, followed by a transition to graphitic N in the NCNT catalysts. Their XPS and electrochemical measurement results indicated that the ORR activity increased with higher graphitic N content but a decrease in pyridinic N. Consequently, Sharifi et al. concluded that graphitic N, especially those so-called valley sites located at the edge of graphene sheets, have higher ORR activity than pyridinic N.[23] It should be pointed out that the total surface N concentrations are not well controlled in these two studies. As discussed by Deng et al.,[20] both graphitic and pyridinic N sites may contribute to the total ORR activity, and the pertinent question is which one is more active than the other. For a fair comparison, the total N concentration in different NCNT samples should remain constant, while the concentrations of these two different types of N doping sites are varied.

Complementary to experiments, first-principles density functional theory (DFT) calculations have been widely applied to predict the activity and mechanism of catalysts.[37,38] Computational predictions at an electronic and molecular scale have been used to explain experimental observations as well as offer guidance to catalyst design.[39,40] Using the DFT method, Gong et al. revealed that the C atoms adjacent to N doping sites, which have a strong electronic affinity, are positively charged and hence become the actual sites for ORR.[3] Furthermore, Zhang et al. performed DFT studies on the reaction pathway of ORR on both graphitic and pyridinic N doping activated C active sites.[41] They predicted that in NCNTs the OOH dissociation pathway of ORR is preferred on these active sites. It should be noted that only a single graphitic N site and a very special pyridinic N site (composed of a cluster of four well-assembled N) were studied by Zhang et al. Consequently, DFT studies of more comprehensive N doping sites are required to identify the most active N doping sites for ORR in NCNTs.

In our studies, we employed a scalable floating catalyst method to synthesize NCNTs catalyst samples containing approximately the same total N surface concentration while the individual doping concentrations of different type active sites are varied. This approach enables us to focus on assessing the effect of different N doping sites as opposed to other studies where both the concentration of different N doping sites and total surface concentration are changed. We additionally complement experimental measurements with detailed theoretical calculations to compare the ORR activity of graphitic and pyridinic N doping in NCNTs. Our calculations suggest that graphitic N activated carbon atoms are the efficient ORR active sites in NCNTs. Our results provide useful insights into the chemical nature of the active sites of ORR in NCNTs and thus enable a strategy for improving the performance of NCNTs for fuel cell application.

2. EXPERIMENTAL METHODS

2.1. Synthesis of N-Doped CNTs. NCNTs were prepared via a simple step floating catalyst chemical vapor deposition (FCCVD) process. A thin layer of alumina film (20 nm) was deposited on a silicon wafer substrate by atomic layer deposition (ALD). Fifty milligrams of ferrocene (98%, Sigma-Aldrich) was dispersed in 4.0 mL of ethylenediamine (99.5%, Sigma-Aldrich). The solution was placed in an alumina crucible boat which was placed near the CVD tube entrance. Argon (99.999%, Matheson) was introduced to the tube, purging at a flow rate of 100 sccm. Then the system was heated to 850 °C at a rate of 30 °C/min. The crucible boat was moved into the CVD furnace after the temperature reached 850 °C. At this temperature, the solution vaporized inside the tube and NCNTs deposited onto the silicon wafer substrate and the wall of quartz tube. The whole system was maintained at 850 °C for 1 h to vaporize all of the solution, and then the furnace was cooled to room temperature. The NCNT forests were peeled off from the substrate and treated with 0.5 M H_2SO_4 solution overnight to remove the metal catalysts. The NCNTs were dried under 75 °C for 2 h. Finally, the NCNT samples were annealed in an alumina crucible under an Ar atmosphere at 800 °C for 1 h to remove the amorphous carbon.

2.2. Morphology Characterization. Morphology characterization of N-doped CNTs was performed using a Zeiss SIGMA VP field-emission scanning electron microscope at 5 kV. Transmission electron microscopy (TEM) was performed by a Hitachi H9500 ETEM at 200 kV. X-ray photoelectron spectroscopy (XPS) analysis was conducted on each sample with the ESCALAB 250Xi (Thermo Scientific) at 14.5 kV. Thermo Scientific Avantage software was applied to perform the data analysis.

2.3. Electrocatalytic Measurements. Electrochemical measurements were performed with a rotating ring−disk electrode system (WD20-RRDE, Pine Instruments). A saturated Ag/AgCl reference electrode was applied, and a Pt plate was used as a counter electrode. The working electrode was prepared by coating a rotating ring−disk glassy carbon disk electrode with the catalyst. The loading amount of commercial 20 wt % Pt/C (Johnson Matthey) is 0.1 mg/cm^2. The glassy carbon (GC) electrode (0.196 cm^2) was polished with alumina paste on a polishing cloth, then rinsed by deionized (DI) water, and dried in the air. A thin layer of NCNTs was then coated from solution (loading of 0.6 mg/cm^2, 5 mg/mL in ethanol with 0.5 wt % Nafion) on the GC electrode. A 0.1 M KOH solution was used as the electrolyte solution for the electrocatalytic measurements. To saturate the electrolyte with O_2 or N_2, the electrolyte was bubbled with O_2 or N_2 for 30 min before electrochemical measurement. The cyclic voltammogram (CV) was conducted with a scan rate of 50 mV/s from 0 to 1.23 V. The electrochemical activity was recorded by using a linear sweep voltammogram (LSV) from 1.23 to 0 V at a scan rate of 5 mV/s at different rotation speeds (100, 400, 900, and 1600 rpm).

2.4. Computational Simulations. The first-principles DFT calculations[42,43] were performed using the Vienna Ab initio Simulation Package (VASP).[44,45] The core electrons were described by the projector augmented wave (PAW) pseudopotential.[46,47] The cutoff energy was set as 400 eV for expanding the wave function. The Perdew, Burke, and Ernzernhof (PBE)[48] functional in the generalized gradient approximation (GGA) was used to describe the electronic exchange correlation. The Brillouin zone was sampled by using Monkhorst−Pack grids[49] of 1 × 1 × 1 for edge-hosted graphitic and pyridinic NCNTs (Figure S4d,e) and 1 × 1 × 10 for other NCNTs in Figure S4, 1 × 3 × 1 for edge-hosted graphitic, and 2 × 5 × 1 for other graphitic NCNTs. The atomic positions were optimized until the forces fell below 0.02 eV/Å. Vacuum thicknesses of at least 13 Å were included in the simulation supercells so that the interactions between adjacent nanotubes were negligible. Zero-point energy corrections were included in all reported results.

https://dx.doi.org/10.1021/acs.jpcc.9b11090
J. Phys. Chem. C 2020, 124, 8689−8696

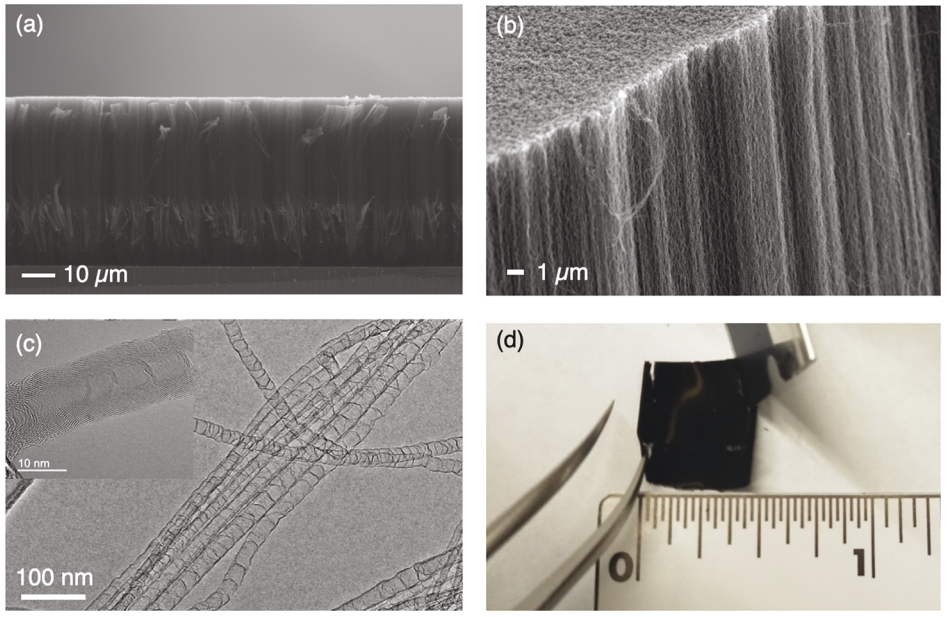

Figure 1. Morphology characterizations of the NCNT samples. (a) SEM side-view image of the as-synthesized NCNTs on the substrate. (b) Tilted NCNTs SEM image. (c) High-resolution TEM image of NCNTs. (d) Optical image of the peeled off NCNTs sheet.

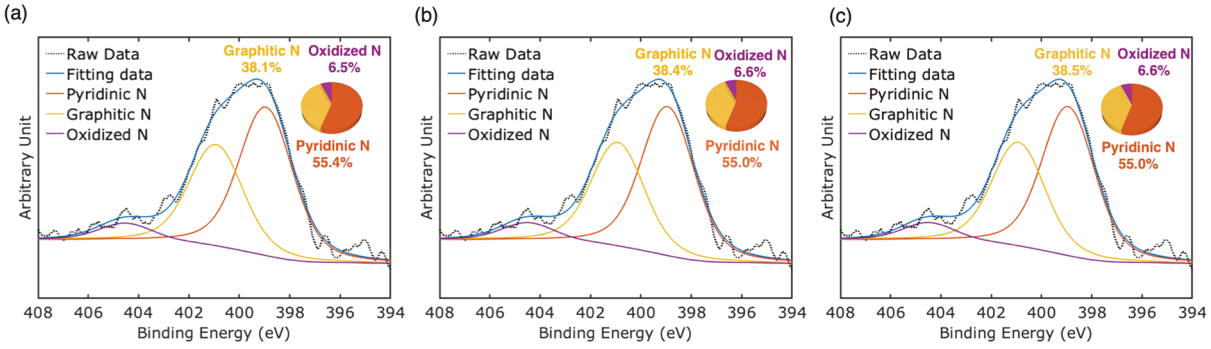

Figure 2. Evaluation of XPS data analysis sensitivity. XPS peak fitting analysis. (a–c) Three XPS deconvolution fitting trials with fixed FWHM.

3. RESULTS AND DISCUSSION

3.1. Physical Characterization of N-Doped CNTs. In this study, N-doped CNTs were synthesized by the floating catalyst method discussed in the previous section. The morphology of the NCNTs is shown in Figure 1. Figure 1a shows a side-view SEM image of the NCNTs. The height of the vertically aligned NCNTs is about 50 μm. The NCNTs are vertically aligned during the growth.[50−53] Figure 1b presents a 10° tilted SEM view of the aligned NCNTs forests to illustrate its well-aligned characteristics. Figure 1c illustrates high-resolution TEM images of NCNTs, showing there are no iron particles after the acid post-treatment process. The inset shows that the NCNTs have a bamboo-like structure similar to other reports[3,54] and are multiwalled with a uniform outer diameter of about 20 nm. The structures are highly crystalline, and no metal impurities were contained within the NCNTs. Figure 1d shows an optical image of the NCNTs forests, which were physically peeled off the substrate prior to transfer for ORR testing.

3.2. X-ray Photoelectron Spectroscopy Analysis. Currently, there is much disagreement in the literature with regard to whether pyridinic N or graphitic N is more responsible for the ORR reactivity of NCNTs. In this paper, we point out that one of the potential sources of discrepancies in the literature may be due to the improper analysis of X-ray photoelectron spectroscopy (XPS) data. The N-doping content and the chemical structure of elements are commonly characterized by XPS, where raw XPS data are smoothed and then subsequently deconvolved into multiple Gaussian−Lorentzian curves. We provide an illustrative example (Figure S1) to show that this XPS analysis may lead to very different interpretations of the data when the raw XPS data consist of a single peak and are deconvolved into multiple Gaussian−Lorentzian curves with independent full width at half-maxima (FHWMs) as can be found in the literature.[20,55−57]

Instead, the FWHM of the photoelectron peaks should be constrained to be the same as those of nearby peaks as the FWHM is correlated to the core-hole lifetime.[58] Figure 2 shows the deconvoluted results of the XPS raw data with the same initial input parameters used in Figure S1, but the FWHM is now fixed to be the same with each other. The analysis is robust, and the same pyridinic to graphitic N ratio is obtained. The deconvolution was shown to be stable with consistently less than 0.1% variation as well as the consistency of peak position and FWHM values with different smoothing methods such as Savitzky−Golay,[59] Fourier,[60] and moving average[61] filter. Furthermore, each NCNT sample was analyzed in nine random locations to obtain statistics on the

https://dx.doi.org/10.1021/acs.jpcc.9b11090
J. Phys. Chem. C 2020, 124, 8689−8696

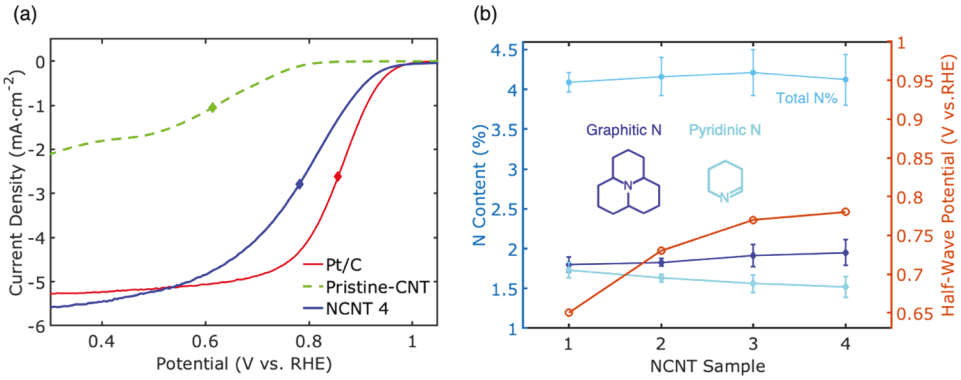

Figure 3. Electrochemical measurement results. (a) LSV curves of Pt/C, pristine CNT, and NCNT4 catalyst samples at a rotation speed of 1600 rpm. (b) N content of four NCNT samples (light blue marker: total N contents; dark blue marker: graphitic N content; cyan marker: pyridinic N content) and half-wave potential (red markers and right *y*-axis).

variation of doping concentration in each sample. Our results are thus based on robust XPS analysis of N functional groups identification.

3.3. Rotating Ring−Disk Electrode (RRDE) Measurements. At present, no fabrication method is capable of precisely controlling or isolating one N functional group. Thus, there are more than one type of N group existing in the sample after chemical synthesis. This poses an issue for extracting a correlation between ORR activity and particular N species when both the total N content and individual N group concentrations are varied. In this case, four NCNTs samples were synthesized by using the same recipe (4.0 mL of EDA) to investigate the role of different doping sites. The total N content is similar (∼4.1%) as shown in Figure 3b. Some studies have indicated that carbon defects also contribute to ORR activity.[62] To verify the consistency of the carbon matrix for all the NCNTs samples, Raman spectroscopy analysis was employed to characterize the defect level (Figure S2). The ratio of I_D/I_G indicates the perfection of the carbon matrix, where I_D and I_G are the intensity of the D and G band in the Raman spectrum, respectively. The results show a consistent I_D/I_G, indicating that the numbers of defects or disorders in the four different synthesized samples are about the same. The samples were assessed by comparing their N doping types and electrocatalytic activity, which were obtained from XPS results and electrochemical measurements, respectively.

The catalytic performances of the four NCNTs samples were characterized by comparing the half-wave potential of rotating ring disk electrode (RRDE) tests at 1600 rpm in alkaline media. The results of RRDE measurements for 20 wt % Pt/C (Johnson Matthey), pristine CNT, and NCNT4 at 1600 rpm are shown in Figure 3a. The half-wave potential is the potential at half of the limiting current density, which is marked in each of the LSV curves. Table 1 summarizes the onset potential, half-wave potential, limiting current density, and number of electrons transferred for the different samples. The number of electrons transferred can be directly obtained from RRDE measurements at 0.3 V (Table 1) or calculated by RRDE measurements at different rotation speeds and Koutecký−Levich equation (Figure S3 and Table S2). Both of these methodologies show good agreement in assessing the number of electrons transferred. The ORR catalytic activity of the NCNT4 sample was found to be similar to commercial Pt/C catalyst in our tests based on the values of the half-wave potential. With the same loading amount and concentration, the NCNT4 sample has almost 3 times the limiting current density compared to undoped CNTs, indicative of a significant increase in catalytic ability. We then performed the analysis on detailed N 1s XPS scans to distinguish the different doping N species in four NCNT samples. The N 1s spectrum was deconvoluted into three Gaussian−Lorentzian functions, corresponding to three N surface functionalities: pyridinic N, graphitic N, and their oxidized forms. Nine random locations were analyzed for each sample.

Table 1. Summary of ORR Catalysis Performance Indicators

catalyst sample	onset potential (V)	half-wave potential (V)	limiting current density (mA/cm^2)	no. of electrons transferred (0.3 V)
NCNT 1	0.90	0.69	−6.15	3.84
NCNT 2	0.92	0.73	−5.09	3.83
NCNT 3	0.94	0.77	−5.20	3.92
NCNT 4	0.96	0.78	−5.82	3.92
Pt/C	1.00	0.86	−5.24	3.99
pristine CNT	0.80	0.61	−2.62	

The summary statistics of the total N, graphitic N, and pyridinic N doping percentage are shown in Figure 3b with different blue curves on the left *y*-axis. The half-wave potential for these four different samples is shown in the right *y*-axis. As shown in Figure 3b, the total N content was maintained across all four samples at ∼4.1%, while the concentration of individual N doping sites was varied. This is in contrast to other papers where both the total and individual N active site concentrations are changing.[19] Our experiments address limitations of analyses where both total and active site N contents are varied by characterizing multiple NCNTs samples with the same approximate total N content. We demonstrated a clear positive correlation only between ORR performance and graphitic N concentration and a negative correlation with pyridinic N, suggesting that graphitic N is the efficient active site for ORR.

3.4. ORR Active Site Model. To further understanding of NCNT ORR catalytic activity, first-principles DFT calculations were performed to predict the limiting electrode potentials of ORR on different N doping sites. Nine different active sites (Figure S4) including a variety of graphitic (*grp*) and pyridinic (*pyd*) sites were analyzed for (5,5) CNTs. Consistent with our experimental results, we assumed a 4e$^-$ pathway, in which the O_2 molecule adsorbs on the C next to N to start ORR and then O_2 is protonated to form OOH, O, OH, and H_2O sequentially. We employed the computational hydrogen electrode method developed by Nørskov et al.[63] and computed the free energies

https://dx.doi.org/10.1021/acs.jpcc.9b11090
J. Phys. Chem. C 2020, 124, 8689−8696

of all elementary steps as a function of electrode potential U with reference to the RHE.

The predicted adsorption energies of all nine sites considered are summarized in Table S3. Here, we highlight the results of these studies by showing the ORR activity of *grp*-eNCNT (a single graphitic N dopant replacing a carbon atom next to the carbon on the edge of CNT), *grp*-bNCNT (a single graphitic N dopant replacing a carbon atom inside CNT), *grp*-p2NCNT (two graphitic N dopants replacing two adjacent C atoms in CNT), and *pyd*-eNCNT (a single pyridinic N dopant replacing a carbon atom on the edge of CNT). The calculated adsorption energies are presented in Table 2. Using these adsorption energies, we plot the free energy evolution of ORR on these four sites. In Figure 4, the limiting potentials of *grp*-eNCNT, *grp*-bNCNT, *grp*-p2NCNT, and *pyd*-eNCNT are 0.76, 0.65, 0.45, and 0.14 V, respectively. In our models, the *grp*-eNCNT shows the best ORR catalytic activity with a 0.76 V onset potential, in good agreement with experimental trends that graphitic N has better ORR activity than pyridinic N. Compared with that of *grp*-bNCNT, a better ORR performance of *grp*-eNCNT is also consistent with the predictions of other computational works.[26] We also calculated multiple local graphitic N models, such as *pyd*-b3NCNT, *grp*-o2NCNT, and *grp*-m2NCNT shown in Figure S4. In these models, *grp*-m2NCNT had an ORR performance with a limiting potential of 0.13 V (Figure S5), which was still close to that of the pyridinic N site. Our DFT calculations support our experimental results that graphitic N doping is the efficient major active site for ORR in NCNT.

Table 2. Predicted Adsorption Energies of Various ORR Species on the Possible Active Sites

E_{ad} (eV)	O_2	OOH	O	OH	H_2O
grp-eNCNT	0.00	−1.03	−3.89	−2.40	
grp-bNCNT	0.49	−1.15	−3.26	−2.48	0.02
grp-p2NCNT	−0.22	−0.58	−3.68	−2.00	0.74
pyd-eNCNT	0.36	−0.28	−3.29	−1.65	

[a]The adsorption energies are calculated as the difference in energy between the adsorption system and the corresponding isolated systems. Hence, a negative value of the adsorption energy indicates attractive interaction between the ORR species and ORR active sites.

Moreover, we employed the DFT computational method to examine some factors that might affect the structure and activity of the active sites for ORR in NCNT. Using synchrotron-based XPS analysis of the N-doped graphene samples after reaction, Xing et al. found the formation of a new structure with OH attached to the carbon atom adjacent to pyridinic N.[22] This experimental finding raises the possibility that the electrochemical ORR condition may lead to the formation of new active site structures containing C, N, and O atoms. To examine this point, we performed DFT predictions of the free energy evolution for ORR on the pyridinic N site with the edge C atom terminated by H (Figure S6a), no termination (Figure S6b), or OH (Figure S6c). First, our results in Figure S6b show that if the edge C atom has no termination group, this carbon atom exhibits strong adsorption to the ORR species and thermodynamically favors the formation of OH termination through a $3e^-$ reaction. This

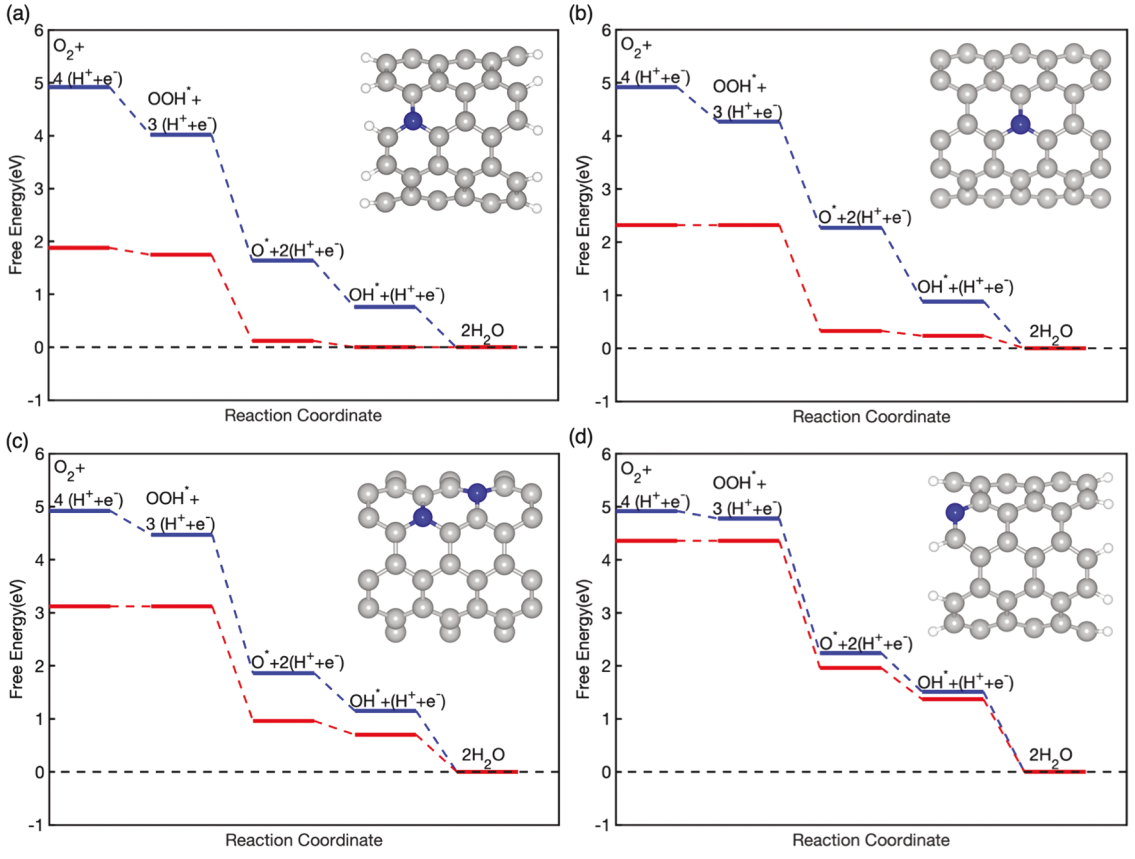

Figure 4. Free energy evolution of ORR on (a) *grp*-eNCNT, (b) *grp*-bNCNT, (c) *grp*-p2NCNT, and (d) *pyd*-eNCNT under electrode potential U = 0 V (blue line) and limiting potential (red line), corresponding to 0.76, 0.65, 0.45, and 0.14 V, respectively.

https://dx.doi.org/10.1021/acs.jpcc.9b11090
J. Phys. Chem. C 2020, 124, 8689−8696

prediction agrees with the observation by Xing et al.[22] However, we predicted that the OH group modification showed only little improvement for ORR activity on the pyridinic N site, as shown in Figure S6c. Consequently, we do not believe that the formation of a new O-containing structure around a pyridinic N site during ORR would make it more active than a graphitic N site in NCNT.

Our DFT results in Figure 4a,d suggest that both graphitic N and pyridinic N sites can promote 4e$^-$ ORR, and graphitic N sites are more efficient than pyridinic N sites in this regard. This theoretical prediction is in support of our experimental results in Figure 3. Furthermore, we performed the DFT calculations to examine how a neighboring N dopants would affect the ORR activity of efficient graphitic N site. In this regard, our results in Figure 4b,c show that a neighboring graphitic N would decrease the limiting potential of the graphitic N site by 0.20 V. Our results in Figure S7 show that a neighboring pyridinic N would also decrease the limiting potential of the graphitic N site by about 0.22 V. Thus, we predict that neighboring N dopants could reduce the ORR activity of the efficient graphitic N sites. Consequently, a good dispersing of N dopants in CNTs is believed to be beneficial for their activity for ORR.

4. CONCLUSIONS

NCNTs were synthesized via the floating catalyst chemical vapor deposition method for ORR catalysts. The correlations between the XPS data and electrochemical measurements indicate that increasing graphitic N and decreasing pyridinic N lead to improvements in electrocatalytic performance. DFT calculations further support this correlation by predicting that graphitic N was the much more efficient active sites for ORR than pyridinic N in alkaline media. The computational approach evaluated a comprehensive number of possible reaction pathways for both CNTs and graphene. We also point out the importance of good XPS analysis practices (i.e., fixed FWHM) for reproducible and reliable chemical composition results. Our experimental and simulations results together indicate the importance of increasing graphitic N rather than pyridinic N density for performance enhancement of NCNTs for fuel cell applications.

■ ASSOCIATED CONTENT

Supporting Information

The Supporting Information is available free of charge at https://pubs.acs.org/doi/10.1021/acs.jpcc.9b11090.

Figures S1−S7 and Tables S1−S3 (PDF)

■ AUTHOR INFORMATION

Corresponding Authors

Guofeng Wang − *Department of Mechanical Engineering and Materials Science, University of Pittsburgh, Pittsburgh, Pennsylvania 15213, United States;* orcid.org/0000-0001-8249-4101; Email: guw8@pitt.edu

Paul W. Leu − *Department of Industrial Engineering, University of Pittsburgh, Pittsburgh, Pennsylvania 15213, United States;* Email: pleu@pitt.edu

Authors

Zhengyu Xu − *Department of Chemical and Petroleum Engineering, University of Pittsburgh, Pittsburgh, Pennsylvania 15213, United States*

Ziyu Zhou − *Department of Mechanical Engineering and Materials Science, University of Pittsburgh, Pittsburgh, Pennsylvania 15213, United States;* orcid.org/0000-0002-1009-9433

Boyang Li − *Department of Mechanical Engineering and Materials Science, University of Pittsburgh, Pittsburgh, Pennsylvania 15213, United States*

Complete contact information is available at: https://pubs.acs.org/10.1021/acs.jpcc.9b11090

Author Contributions

Z.Xu and Z.Zhou shared the first authorship and contributed equally to this work. All authors have given approval to the final version of the manuscript.

Notes

The authors declare no competing financial interest.

■ ACKNOWLEDGMENTS

P.W.L. and Z.Z. acknowledge support from U.S. National Science Foundation (NSF ECCS #1552712). G.W. and B.L. acknowledge support from U.S. National Science Foundation (NSF CBET #1804534). G.W. also gratefully acknowledges the computational resources provided by the University of Pittsburgh Center for Research Computing as well as the Extreme Science and Engineering Discovery Environment (XSEDE), which is supported by National Science Foundation Grant ACI-1053575.

■ REFERENCES

(1) Calvin, M. The platinum electrode as a catalyst for the activation of hydrogen. *Trans. Faraday Soc.* **1936**, *32*, 1428−1436.

(2) Holton, O. T.; Stevenson, J. W. The role of platinum in proton exchange membrane fuel cells. *Platinum Met. Rev.* **2013**, *57*, 259−271.

(3) Gong, K.; Du, F.; Xia, Z.; Durstock, M.; Dai, L. Nitrogen-doped carbon nanotube arrays with high electrocatalytic activity for oxygen reduction. *Science* **2009**, *323*, 760−764.

(4) Sealy, C. The problem with platinum. *Mater. Today* **2008**, *11*, 65−68.

(5) Holewinski, A.; Idrobo, J.-C.; Linic, S. High-performance Ag-Co alloy catalysts for electrochemical oxygen reduction. *Nat. Chem.* **2014**, *6*, 828.

(6) Dai, L.; Xue, Y.; Qu, L.; Choi, H.-J.; Baek, J.-B. Metal-free catalysts for oxygen reduction reaction. *Chem. Rev.* **2015**, *115*, 4823−4892.

(7) Bashyam, R.; Zelenay, P. A class of non-precious metal composite catalysts for fuel cells. *Nature* **2006**, *443*, 63.

(8) Lu, S.; Pan, J.; Huang, A.; Zhuang, L.; Lu, J. Alkaline polymer electrolyte fuel cells completely free from noble metal catalysts. *Proc. Natl. Acad. Sci. U. S. A.* **2008**, *105*, 20611−20614.

(9) Su, D. S.; Sun, G. Nonprecious-Metal Catalysts for Low-Cost Fuel Cells. *Angew. Chem., Int. Ed.* **2011**, *50*, 11570−11572.

(10) Nagaiah, T. C.; Kundu, S.; Bron, M.; Muhler, M.; Schuhmann, W. Nitrogen-doped carbon nanotubes as a cathode catalyst for the oxygen reduction reaction in alkaline medium. *Electrochem. Commun.* **2010**, *12*, 338−341.

(11) Chen, S.; Bi, J.; Zhao, Y.; Yang, L.; Zhang, C.; Ma, Y.; Wu, Q.; Wang, X.; Hu, Z. Nitrogen-doped carbon nanocages as efficient metal-free electrocatalysts for oxygen reduction reaction. *Adv. Mater.* **2012**, *24*, 5593−5597.

(12) Tian, G.-L.; Zhao, M.-Q.; Yu, D.; Kong, X.-Y.; Huang, J.-Q.; Zhang, Q.; Wei, F. Nitrogen-doped graphene/carbon nanotube hybrids: in situ formation on bifunctional catalysts and their superior electrocatalytic activity for oxygen evolution/reduction reaction. *Small* **2014**, *10*, 2251−2259.

(13) Shui, J.; Wang, M.; Du, F.; Dai, L. N-doped carbon nanomaterials are durable catalysts for oxygen reduction reaction in acidic fuel cells. *Science advances* **2015**, *1*, e1400129.
(14) Chen, P.; Xiao, T.-Y.; Qian, Y.-H.; Li, S.-S.; Yu, S.-H. A Nitrogen-doped graphene/carbon nanotube nanocomposite with synergistically enhanced electrochemical activity. *Adv. Mater.* **2013**, *25*, 3192−3196.
(15) Guo, D.; Shibuya, R.; Akiba, C.; Saji, S.; Kondo, T.; Nakamura, J. Active sites of nitrogen-doped carbon materials for oxygen reduction reaction clarified using model catalysts. *Science* **2016**, *351*, 361−365.
(16) Kundu, S.; Nagaiah, T. C.; Xia, W.; Wang, Y.; Dommele, S. V.; Bitter, J. H.; Santa, M.; Grundmeier, G.; Bron, M.; Schuhmann, W. Electrocatalytic Activity and Stability of Nitrogen-Containing Carbon Nanotubes in the Oxygen Reduction Reaction. *J. Phys. Chem. C* **2009**, *113*, 14302−14310.
(17) Chen, Z.; Higgins, D.; Tao, H.; Hsu, R. S.; Chen, Z. Highly active nitrogen-doped carbon nanotubes for oxygen reduction reaction in fuel cell applications. *J. Phys. Chem. C* **2009**, *113*, 21008−21013.
(18) Higgins, D.; Chen, Z.; Chen, Z. Nitrogen doped carbon nanotubes synthesized from aliphatic diamines for oxygen reduction reaction. *Electrochim. Acta* **2011**, *56*, 1570−1575.
(19) Rao, C. V.; Cabrera, C. R.; Ishikawa, Y. In search of the active site in nitrogen-doped carbon nanotube electrodes for the oxygen reduction reaction. *J. Phys. Chem. Lett.* **2010**, *1*, 2622−2627.
(20) Deng, H.; Li, Q.; Liu, J.; Wang, F. Active sites for oxygen reduction reaction on nitrogen-doped carbon nanotubes derived from polyaniline. *Carbon* **2017**, *112*, 219−229.
(21) Liu, J.; Song, P.; Xu, W. Structure-activity relationship of doped-nitrogen (N)-based metal-free active sites on carbon for oxygen reduction reaction. *Carbon* **2017**, *115*, 763−772.
(22) Xing, T.; Zheng, Y.; Li, L. H.; Cowie, B. C.; Gunzelmann, D.; Qiao, S. Z.; Huang, S.; Chen, Y. Observation of active sites for oxygen reduction reaction on nitrogen-doped multilayer graphene. *ACS Nano* **2014**, *8*, 6856−6862.
(23) Sharifi, T.; Hu, G.; Jia, X.; Wågberg, T. Formation of active sites for oxygen reduction reactions by transformation of nitrogen functionalities in nitrogen-doped carbon nanotubes. *ACS Nano* **2012**, *6*, 8904−8912.
(24) Niwa, H.; Horiba, K.; Harada, Y.; Oshima, M.; Ikeda, T.; Terakura, K.; Ozaki, J.-i.; Miyata, S. X-ray absorption analysis of nitrogen contribution to oxygen reduction reaction in carbon alloy cathode catalysts for polymer electrolyte fuel cells. *J. Power Sources* **2009**, *187*, 93−97.
(25) Liu, R.; Wu, D.; Feng, X.; Müllen, K. Nitrogen-doped ordered mesoporous graphitic arrays with high electrocatalytic activity for oxygen reduction. *Angew. Chem.* **2010**, *122*, 2619−2623.
(26) Kim, H.; Lee, K.; Woo, S. I.; Jung, Y. On the mechanism of enhanced oxygen reduction reaction in nitrogen-doped graphene nanoribbons. *Phys. Chem. Chem. Phys.* **2011**, *13*, 17505−17510.
(27) Wang, N.; Lu, B.; Li, L.; Niu, W.; Tang, Z.; Kang, X.; Chen, S. Graphitic nitrogen is responsible for oxygen electroreduction on nitrogen-doped carbons in alkaline electrolytes: Insights from activity attenuation studies and theoretical calculations. *ACS Catal.* **2018**, *8*, 6827−6836.
(28) Yang, J.; Sun, H.; Liang, H.; Ji, H.; Song, L.; Gao, C.; Xu, H. A highly efficient metal-free oxygen reduction electrocatalyst assembled from carbon nanotubes and graphene. *Adv. Mater.* **2016**, *28*, 4606−4613.
(29) Tao, L.; Wang, Q.; Dou, S.; Ma, Z.; Huo, J.; Wang, S.; Dai, L. Edge-rich and dopant-free graphene as a highly efficient metal-free electrocatalyst for the oxygen reduction reaction. *Chem. Commun.* **2016**, *52*, 2764−2767.
(30) Futaba, D. N.; Hata, K.; Yamada, T.; Hiraoka, T.; Hayamizu, Y.; Kakudate, Y.; Tanaike, O.; Hatori, H.; Yumura, M.; Iijima, S. Shape-engineerable and highly densely packed single-walled carbon nanotubes and their application as super-capacitor electrodes. *Nat. Mater.* **2006**, *5*, 987−994.
(31) Zou, X.; Wang, L.; Yakobson, B. I. Mechanisms of the oxygen reduction reaction on B-and/or N-doped carbon nanomaterials with curvature and edge effects. *Nanoscale* **2018**, *10*, 1129−1134.
(32) Sabatier, P. Hydrogénations et déshydrogénations par catalyse. *Ber. Dtsch. Chem. Ges.* **1911**, *44*, 1984−2001.
(33) Gíslason, P. M.; Skúlason, E. Catalytic trends of nitrogen doped carbon nanotubes for oxygen reduction reaction. *Nanoscale* **2019**, *11*, 18683−18690.
(34) Hu, R.; Wu, C.; Hou, K.; Xia, C.; Yang, J.; Guan, L.; Li, Y. Tailoring the electrocatalytic oxygen reduction reaction pathway by tuning the electronic states of single-walled carbon nanotubes. *Carbon* **2019**, *147*, 35−42.
(35) Zhang, R.; Zhang, Y.; Zhang, Q.; Xie, H.; Qian, W.; Wei, F. Growth of half-meter long carbon nanotubes based on Schulz-Flory distribution. *ACS Nano* **2013**, *7*, 6156−6161.
(36) Hata, K.; Futaba, D. N.; Mizuno, K.; Namai, T.; Yumura, M.; Iijima, S. Water-assisted highly efficient synthesis of impurity-free single-walled carbon nanotubes. *Science* **2004**, *306*, 1362−1364.
(37) Duan, Z.; Wang, G. Comparison of reaction energetics for oxygen reduction reactions on Pt (100), Pt (111), Pt/Ni (100), and Pt/Ni (111) surfaces: a first-principles study. *J. Phys. Chem. C* **2013**, *117*, 6284−6292.
(38) Kattel, S.; Wang, G. Reaction pathway for oxygen reduction on FeN4 embedded graphene. *J. Phys. Chem. Lett.* **2014**, *5*, 452−456.
(39) Seh, Z. W.; Kibsgaard, J.; Dickens, C. F.; Chorkendorff, I.; Nørskov, J. K.; Jaramillo, T. F. Combining theory and experiment in electrocatalysis: Insights into materials design. *Science* **2017**, *355*, eaad4998.
(40) Kulkarni, A.; Siahrostami, S.; Patel, A.; Nørskov, J. K. Understanding catalytic activity trends in the oxygen reduction reaction. *Chem. Rev.* **2018**, *118*, 2302−2312.
(41) Zhang, P.; Lian, J.; Jiang, Q. Potential dependent and structural selectivity of the oxygen reduction reaction on nitrogen-doped carbon nanotubes: a density functional theory study. *Phys. Chem. Chem. Phys.* **2012**, *14*, 11715−11723.
(42) Kohn, W.; Sham, L. J. Self-consistent equations including exchange and correlation effects. *Phys. Rev.* **1965**, *140*, A1133.
(43) Hohenberg, P.; Kohn, W. Inhomogeneous electron gas. *Phys. Rev.* **1964**, *136*, B864.
(44) Kresse, G.; Furthmüller, J. Efficiency of ab-initio total energy calculations for metals and semiconductors using a plane-wave basis set. *Comput. Mater. Sci.* **1996**, *6*, 15−50.
(45) Kresse, G. Ab initio molecular dynamics for liquid metals. *J. Non-Cryst. Solids* **1995**, *192*, 222−229.
(46) Kresse, G.; Joubert, D. From ultrasoft pseudopotentials to the projector augmented-wave method. *Phys. Rev. B: Condens. Matter Mater. Phys.* **1999**, *59*, 1758.
(47) Blöchl, P. E. Projector augmented-wave method. *Phys. Rev. B: Condens. Matter Mater. Phys.* **1994**, *50*, 17953.
(48) Perdew, J. P.; Burke, K.; Ernzerhof, M. Generalized gradient approximation made simple. *Phys. Rev. Lett.* **1996**, *77*, 3865.
(49) Monkhorst, H. J.; Pack, J. D. Special points for Brillouin-zone integrations. *Phys. Rev. B* **1976**, *13*, 5188.
(50) Roy, S.; David-Pur, M.; Hanein, Y. Carbon nanotube growth inhibition in floating catalyst based chemical vapor deposition and its application in flexible circuit fabrication. *Carbon* **2017**, *116*, 40−49.
(51) Schneider, J. J. Vertically aligned carbon nanotubes as platform for biomimetically inspired mechanical sensing, bioactive surfaces, and electrical cell interfacing. *Advanced Biosystems* **2017**, *1*, 1700101.
(52) Mikhalchan, A.; Fan, Z.; Tran, T. Q.; Liu, P.; Tan, V. B.; Tay, T.-E.; Duong, H. M. Continuous and scalable fabrication and multifunctional properties of carbon nanotube aerogels from the floating catalyst method. *Carbon* **2016**, *102*, 409−418.
(53) Xiang, R.; Yang, Z.; Zhang, Q.; Luo, G.; Qian, W.; Wei, F.; Kadowaki, M.; Einarsson, E.; Maruyama, S. Growth deceleration of vertically aligned carbon nanotube arrays: Catalyst deactivation or feedstock diffusion controlled? *J. Phys. Chem. C* **2008**, *112*, 4892−4896.

https://dx.doi.org/10.1021/acs.jpcc.9b11090
J. Phys. Chem. C 2020, 124, 8689−8696

(54) Liu, H.; Zhang, Y.; Li, R.; Sun, X.; Désilets, S.; Abou-Rachid, H.; Jaidann, M.; Lussier, L.-S. Structural and morphological control of aligned nitrogen-doped carbon nanotubes. *Carbon* **2010**, *48*, 1498−1507.
(55) Liu, J.; Song, P.; Xu, W. Structure-activity relationship of doped-nitrogen (N)-based metal-free active sites on carbon for oxygen reduction reaction. *Carbon* **2017**, *115*, 763−772.
(56) Chen, Z.; Higgins, D.; Chen, Z. Nitrogen doped carbon nanotubes and their impact on the oxygen reduction reaction in fuel cells. *Carbon* **2010**, *48*, 3057−3065.
(57) Lai, L.; Potts, J. R.; Zhan, D.; Wang, L.; Poh, C. K.; Tang, C.; Gong, H.; Shen, Z.; Lin, J.; Ruoff, R. S. Exploration of the active center structure of nitrogen-doped graphene-based catalysts for oxygen reduction reaction. *Energy Environ. Sci.* **2012**, *5*, 7936−7942.
(58) van der Heide, P. *X-ray Photoelectron Spectroscopy: An introduction to Principles and Practices*; John Wiley & Sons: 2011.
(59) Madden, H. H. Comments on the Savitzky-Golay convolution method for least-squares-fit smoothing and differentiation of digital data. *Anal. Chem.* **1978**, *50*, 1383−1386.
(60) Proctor, A.; Sherwood, P. M. Data analysis techniques in x-ray photoelectron spectroscopy. *Anal. Chem.* **1982**, *54*, 13−19.
(61) Proctor, A.; Sherwood, P. M. Smoothing of digital X-ray photoelectron spectra by an extended sliding least-squares approach. *Anal. Chem.* **1980**, *52*, 2315−2321.
(62) Yan, X.; Jia, Y.; Yao, X. Defects on carbons for electrocatalytic oxygen reduction. *Chem. Soc. Rev.* **2018**, *47*, 7628−7658.
(63) Nørskov, J. K.; Rossmeisl, J.; Logadottir, A.; Lindqvist, L.; Kitchin, J. R.; Bligaard, T.; Jonsson, H. Origin of the overpotential for oxygen reduction at a fuel-cell cathode. *J. Phys. Chem. B* **2004**, *108*, 17886−17892.

https://dx.doi.org/10.1021/acs.jpcc.9b11090
J. Phys. Chem. C 2020, 124, 8689−8696